ACS OMEGA

http://pubs.acs.org/journal/acsodf

Article

Synthesis of Hollow N,P-Doped Carbon/$Co_2P_2O_7$ Nanotubular Crystals as an Effective Electrocatalyst for the Oxygen Reduction Reaction

Yanhua Lei,* Da Huo, Mengchao Ding, Fei Zhang, Ruixuan Yu, Yuliang Zhang, and Hailiang Du*

Cite This: *ACS Omega* 2022, 7, 5751−5763

Read Online

ACCESS | Metrics & More | Article Recommendations | Supporting Information

ABSTRACT: Herein, N,P-rich carbon/carbon/$Co_2P_2O_7$ hollow nanotubes with a multilayered wall structure were successfully fabricated for the ORR electrocatalyst. The hollow tube structure catalysts were obtained by carbonizing $Co_2P_2O_7$/C coated with the phytate-doped PANI. The $Co_2P_2O_7$/C was obtained by phosphorylating a basic cobalt carbonate with phytic acid (PA). Onset and positive half-wave potentials were measured at 0.90 and 0.84 V, respectively, with a diffusion-limited current density of 4.58 mA/cm^2. Effect of the thickness of polyaniline (PANI) in the electrocatalyst precursor was also investigated. The specific surface area as well as the content of graphitic N altered as the time of PANI polymerization increased, resulting in remarkably different catalytic activities. This study of hollow nanotube catalysts exhibits efficient noble-metal-free oxygen reduction reaction electrocatalysts for other chemical systems, which will provide abundant electrochemical active centers and sufficient energy.

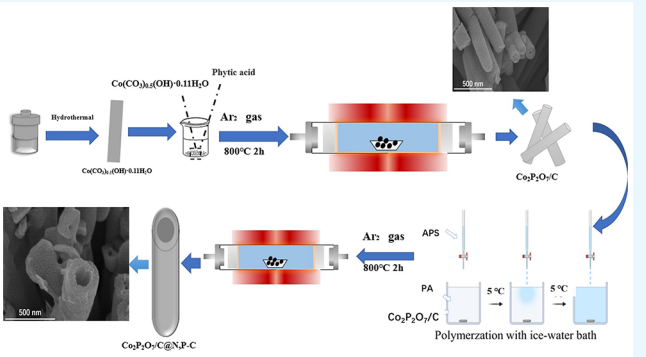

1. INTRODUCTION

Scientists are exploring new energy alternatives, such as solar energy and electrochemical energy, to combat environmental pollution and the current energy crisis.[1−3] In various electrochemical energy systems, fuel cells have received a lot of attention due to their high energy conversion efficiency, high specific energy, low environmental impact, and high reliability. Several factors limit the use of fuel cells on a large scale, including the poor reaction kinetics of the oxygen reduction reaction (ORR) on the cathode[4] and the use of noble metal catalysts.[4−6] Thus, to address the scarcity and high cost of noble-metal-based catalysts, nonmetallic electrocatalysts,[7,8] nonprecious metal catalysts,[9−12] and low noble metal catalysts[13,14] have therefore been investigated and inspected.

Among the various alternatives, transition-metal phosphates are regarded as potential alternatives due to their good electrical conductivity, low price, stable properties, and environmental friendliness. The performance of pyrophosphates of divalent metals with the general formula $M_2P_2O_7$ (M1/4 Co, Ni, etc.) is expected to be a promising material of choice for fuel cells.[15] Heteroatom codoping (for example, boron, nitrogen, phosphorus, sulfur, and others) can considerably improve conductivity and functionality while disrupting the initial conjugated electron coordination environment and even achieve metallicity.[16−20] Taking Co-based materials as examples, most zeolite-imidazole framework (ZIF)-based precursors were used to develop active and nonvolatile bimetallic ZIF-derived catalysts to enhance the performance of oxygen reduction. Wang prepared CS Co@NC-700 and Co@Co_4N/MnO-NC catalysts using Zn and Mn bimetallic MOFs as precursors, respectively, which not only enhanced the performance of ORR but also acted on Zn-ion batteries to improve their stability.[21,22]

As one of the Co−P materials, $Co_2P_2O_7$ has superior performance in supercapacitors, magnetism, microwave absorption, and multiphase catalysis.[23,24] In general, $Co_2P_2O_7$ is mostly used for testing OER mainly stemming from the fact that the valence electron density within the Co center of $Co_2P_2O_7$ decreases significantly when the metal undergoes carbonization. However, the performance of $Co_2P_2O_7$ in ORR catalytic performance was far from expectations. It has been reported that the catalytic performance of catalytic materials can be improved through structural design and composition optimization. Graphene nanocages doped with N,P and $Co_2P_2O_7$ act as Mott−Schottky heterojunction electrocatalysts to enhance their interfacial[25] and thus drive their intrinsic

Received: October 8, 2021
Accepted: January 28, 2022
Published: February 9, 2022

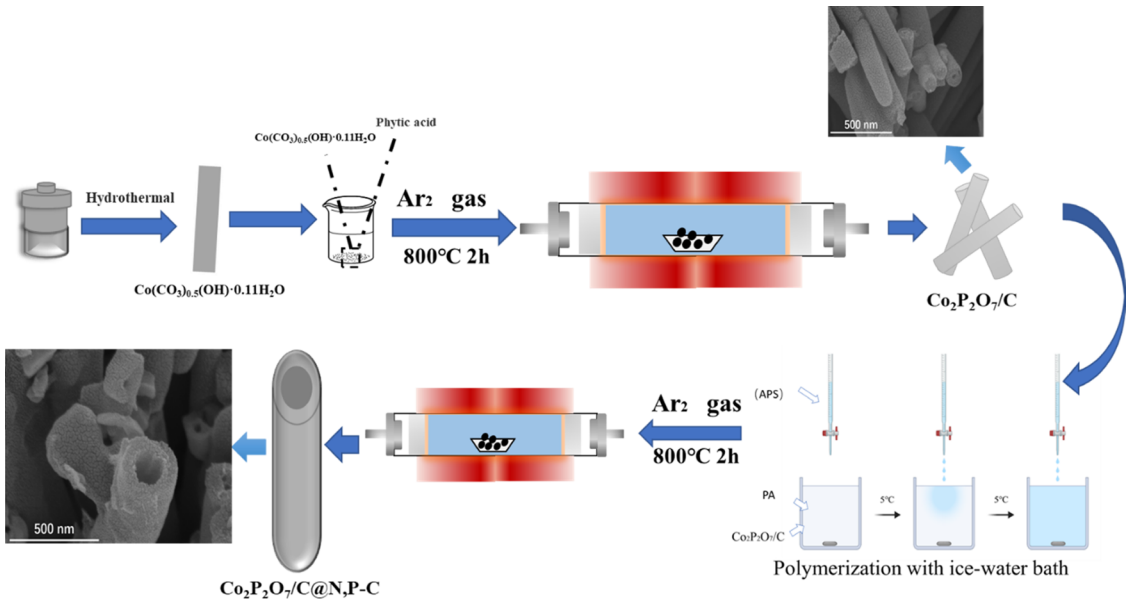

Figure 1. Schematic illustration of the formation of $Co_2P_2O_7$/C@N,P−C.

catalytic activity. The resulting N,P-doped carbon layer having a metallic nature not only regulates the overfilling of the Co center, for example, the orbitals occupied by the $Co_2P_2O_7$ nanorods (NRs) as cocatalysts, but also ensures continuous and long-term operation.[26] However, the smart structure design and synthesis of heterojunction-based $Co_2P_2O_7$ and N,P-codoped carbon nanostates for electrocatalysts with enhanced performance are problems that urgently need to be addressed.

Herein, hollow nanotube (HNTs) catalysts of N,P-rich carbon/carbon/$Co_2P_2O_7$ ($Co_2P_2O_7$/C@N,P−C) were successfully fabricated by combining the advantages of both heteroatom-doped carbon materials and transition-metal phosphides to realize the multifunctionality of the catalyst by carbonizing the PANI-coated $Co_2P_2O_7$. The effect of PANI amount varying by the polymerization time in the catalyst precursor on the catalytic performance was also investigated. The as-prepared catalysts exhibited a much higher electrocatalytic performance and stability for ORR.

2. EXPERIMENTAL SECTION

The steps needed for electrocatalyst syntheses are depicted in Figure 1. $Co_2P_2O_7$/C nanorods were fabricated first by PA-coated chemical $Co(CO_3)_{0.5}(OH)\cdot 0.11H_2O$ carbonization. The final N,P-rich carbon-coated $Co_2P_2O_7$/C catalysts were produced in an in situ reaction through high-temperature carbonization and PANI polymerization.

2.1. Synthesis of $Co(CO_3)_{0.5}(OH)\cdot 0.11H_2O$. In 30 mL of deionized water (DI), dissolution of urea (0.0902 g, 1.5 mmol) and $Co(NO_3)_2\cdot 6H_2O$ (0.1455 g, 0.5 mmol) took place. After 1 h of continuous stirring, the formed light-pink solution was transferred to a stainless steel autoclave composed of poly(tetrafluoroethylene) and placed in an electric oven at 120 °C for 12 h. The resulting precipitates were then subjected to centrifugation followed by washing with DI water after cooling, and $Co(CO_3)_{0.5}(OH)\cdot 0.11H_2O$ was collected as a light-pink solid powder after drying in an oven at 60 °C.

2.2. Synthesis of $Co_2P_2O_7$/C NRs. $Co_2P_2O_7$/C nanorods were synthesized by dissolving 0.1 g of $Co(CO_3)_{0.5}(OH)\cdot 0.11H_2O$ prepared above in 10 mmol/L (50 mL) of PA solution and stirring at 60 °C for 1 h. The precipitate was then collected and dried before being annealed in an Ar atmosphere at 800 °C for 2 h at a heating rate of 5 °C/min from room temperature. The resultant samples were labeled $Co_2P_2O_7$/C NRs.

2.3. Synthesis of N,P-Rich Carbon-Coated $Co_2P_2O_7$/C Hollow Nanotubes (HNTs). First, 0.1 g of $Co_2P_2O_7$/C NRs was placed in a 50 mL PA 10 mM solution in a bilayer flask. The temperature of the flask was cooled to 0−5 °C by a recirculating cooling pump. Then, 0.1 mL of aniline monomer was injected into the solution. After that, 0.1 g of ammonium persulfate (APS) as an oxidant was sonicated in 50 mL of a 10 mM PA solution and dropped into the bilayer flask at a constant rate using a constant pressure drop funnel. The polymerization reaction was carried out for 3−5 h at 5 °C with constant stirring. The PANI-coated $Co_2P_2O_7$ NR product (PANI-co-$Co_2P_2O_7$/C) was filtered and rinsed multiple times with DI before drying in a vacuum at 60 °C. Subsequently, the PANI-co-$Co_2P_2O_7$/C was annealed for 2 h at 800 °C in an Ar atmosphere at a heating rate of 5 °C/min. The resultant N,P-rich carbon-coated $Co_2P_2O_7$/C samples were labeled $Co_2P_2O_7$/C@N,P−C HNTs. For comparison, the catalyst of PANI-derived N,P-doped carbon was obtained by paralyzing the phytate-doped PANI free from the presence of $Co_2P_2O_7$ at 800 °C for 2 h.

2.4. Material Characterizations. An X-ray diffraction (XRD) device of the Bruker D8-advance model was used at 40 mA and 40 kV with a 2θ range of 5−90° to analyze the XRD of the catalysts. The X-ray photon spectra (XPS) were collected using a JPS-9200 instrument supplemented with the radiation of Mg Ka. The Bunko−Keiki M30-TP-M setup was used to perform Raman spectroscopy with a polychromator using YVO_4 532 nm laser for excitation. Investigation of the thermal stability of specimens was carried out through the Perkin Elmer Diamond TG/DTA Lab system's thermogravimetry (TG). The specimens were heated up to 1000 °C at the rate of 10 °C/min under a constant N_2 flow of 50 mL/min. Transmission electron microscopy (TEM) and scanning electron microscopy (SEM) were performed under the JEOL-2010F and JEOL JSM-6510LA instruments, respectively.

https://doi.org/10.1021/acsomega.1c05608
ACS Omega 2022, 7, 5751−5763

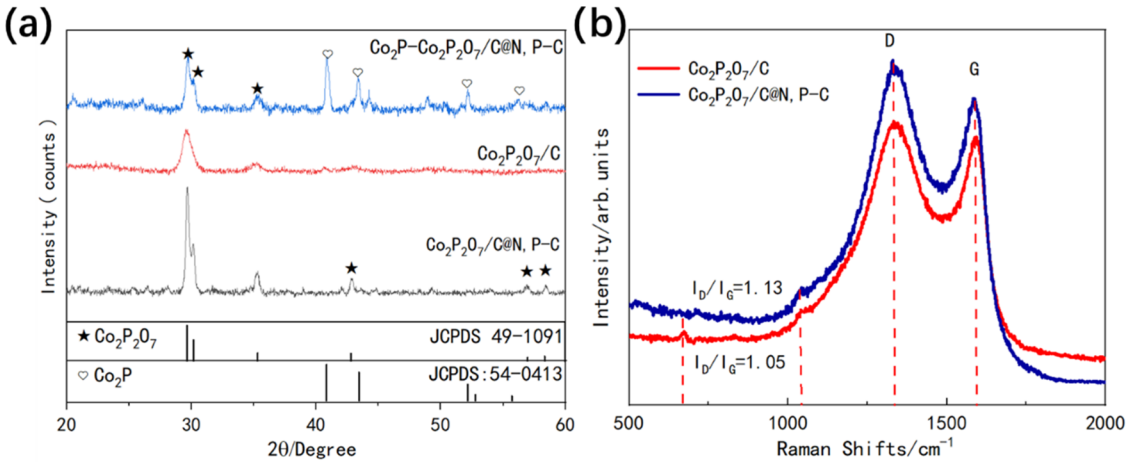

Figure 2. (a) Patterns of XRD for $Co_2P_2O_7$/C, $Co_2P_2O_7$/C@N,P−C, and Co_2P-$Co_2P_2O_7$/C@N,P−C. (b) Raman spectra of $Co_2P_2O_7$/C and $Co_2P_2O_7$/C@N,P−C.

Porosity and specific surface area were calculated employing data from an ASAP-2000 device utilizing the Horvath−Kawazoe (HK) and Brunner−Emmet−Teller (BET) methods. The electrical conductivity measurements of the composite particles were performed using an ST2253 digital four-probe resistance tester (Suzhou Jingge Electronics Co., Ltd.) at room temperature.

2.5. Electrochemical Analysis. The electrocatalytic performance of the as-prepared samples was evaluated with cyclic voltammetry (CV) and linear sweep voltammetry (LSV) tests on a Gamry workstation connected with a rotating disc setup. Rotating discs and rotation ring-disk electrodes (RRDEs) (PINE) were used to assess the electrochemical catalytic performance. The electrolyte used in this experiment was 0.1 mol/L KOH solution, and the working electrode was a glassy carbon disc with a diameter of about 5 mm equipped with an electrocatalyst, while the reference and counter electrodes were an Ag/AgCl solution using 0.1 mol/L KOH and a platinum wire, respectively. A two-channel Gamry 1010E constant potential meter was used for the rotating disc ring device. For testing, a cleaned reaction cell was used and the electrolyte was passed through oxygen until oxygen saturation; the working electrode was polished and cleaned, and a drop of catalyst ink was applied. The catalyst ink was composed of 2 mg of catalysts, ethanol (400 μL), and Nafion (25 μL, 5 wt %). The working electrode had 0.2 mg/cm^2 catalyst loading density. Also, the specific tests can be found in a previous work of our group.[27] The catalytic electrode was first activated by CV performed at 0−1.2 V (vs reversible hydrogen electrode (RHE)) at a 50 mV/s scanning rate in an O_2-saturated 0.1 M KOH solution until a steady curve was observed. LSV was collected in the 0−1.2 V range (vs RHE) at 10 mV/s rate in the O_2-saturated 0.1 M KOH at 100, 400, 900, 1225, 1600, 2000, 2025, and 2500 rpm. All ORR tests were carried out in the presence of a constant oxygen gas stream.

The way to prepare the RRED electrode is to apply a potential of 0.5 V to the Pt ring electrode. Based on the data obtained by RRED, the number of electrons transferred during ORR, n, and the H_2O_2 yield are determined by the following equations.

$$H_2O_2\% = 200 \times \frac{I_R/N}{\frac{I_R}{N} + I_D} \quad (1)$$

$$n = 4 \times \frac{I_D}{\frac{I_R}{N} + I_D} \quad (2)$$

where I_D and I_R are the disk and the ring currents, respectively, and N is the current collection efficiency (equal to 0.37).

All of the potential values were measured relative to the Ag/AgCl potential and were recalculated to the RHE scale using the Nernst equation below

$$E(\text{RHE}) = E\left(\frac{\text{Ag}}{\text{AgCl}}\right) + 0.0591\ \text{pH} + 0.197 \quad (3)$$

3. RESULTS AND DISCUSSION

3.1. Synthesis and Characterization of $Co_2P_2O_7$/C@N,P−C HNTs. The hollowed $Co_2P_2O_7$/C@N,P−C NTs were synthesized through carbonizing the PANI-coated $Co_2P_2O_7$, and the $Co_2P_2O_7$ was obtained by paralyzing the PA-surrounded $Co(CO_3)_{0.5}(OH)\cdot 0.11H_2O$ NRs, schematically illustrated in Figure 1. Specifically, the $Co(CO_3)_{0.5}(OH)\cdot 0.11H_2O$ clubs with widths of 100−200 nm were first synthesized from $Co(NO_3)_2\cdot 6H_2O$ and urea. Then, PA with a high P-content was allowed to coat on the surface of $Co(CO_3)_{0.5}(OH)\cdot 0.11H_2O$ with the help of electrostatic attraction. Subsequently, the protonated PA will react with $Co(CO_3)_{0.5}(OH)\cdot 0.11H_2O$ and form the coordination of Co^{2+} and phytate (Co-phytate). $Co_2P_2O_7$/C was achieved after carbonization of phytate/$Co(CO_3)_{0.5}(OH)\cdot 0.11H_2O$. Then, PANI was polymerized on the surface of $Co_2P_2O_7$/C from the PA-containing solution. Finally, hollow-tube-structured $Co_2P_2O_7$/C@N,P−C catalysts are achieved, after calcination, in which PANI acts as the C,N source, while PA acts as the P source.

Powder XRD was employed to ascertain the sample's crystal structure and phase purity. The XRD outcomes in Figure 2a indicated that the products for the samples with the PA cladding pretreatment and PA cladding treatment followed by PANI were composed of $Co_2P_2O_7$. Other than the peaks of diffraction related to $Co_2P_2O_7$ (JCPDS No. 49-1091), no impurities could be found in the XRD pattern. The main diffraction and peaks at 29.6, 30.1, 35.3, 43.7, 49.3 and 58.3° could be assigned to the (012), (-$\bar{3}$02), (130), (032), (-424) and (-$\bar{1}$34) facets of the $Co_2P_2O_7$ phase, respectively. Further, as shown in Figure 2a, the intensity of the $Co_2P_2O_7$/C@N,P−

https://doi.org/10.1021/acsomega.1c05608
ACS Omega 2022, 7, 5751−5763

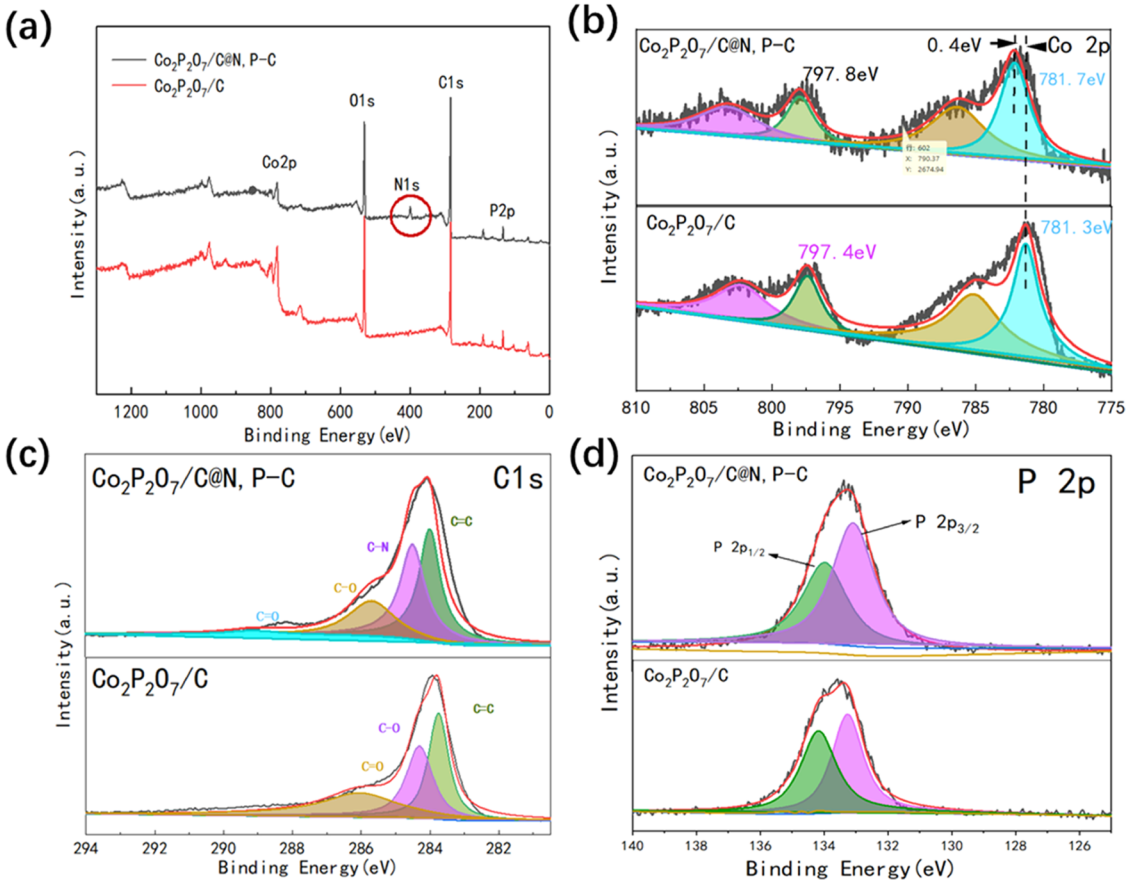

Figure 3. (a) Survey of XPS, (b) Co 2p spectra of $Co_2P_2O_7$/C and $Co_2P_2O_7$/C@N,P−C samples. C 1s (c) and P 2p (d) spectra of $Co_2P_2O_7$/C@N,P−C.

C diffraction peak is significantly higher than that of $Co_2P_2O_7$/C after the introduction of the conducting polymer. This indicates that the crystallinity of the nanotubule is improved. However, it is interesting that, when carbonizing the PANI-PA-coated Co-$(CO_3)_{0.5}(OH)\cdot 0.11H_2O$ without the PA cladding pretreatment, the calcination product was composed of $Co_2P_2O_7$ and Co_2P. The peaks around 40.7, 43.3, 52, and 54.1° are related to the (121), (211), (130), and (002) crystallographic planes of Co_2P, respectively (JCPDS No. 54-0413). Further, we adopted the solution of bicarbonization to obtain the hollow-structured $Co_2P_2O_7$/C@N,P−C NT catalysts.

Figure 2b shows Raman spectra of $Co_2P_2O_7$/C and $Co_2P_2O_7$/C@N,P−C samples. The symmetric stretching vibrations vs PO_3 were attributed to the weak peak at 1033 cm^{-1}, while the POP bridge in $Co_2P_2O_7$ was related to the peak at 674 cm^{-1},[28] confirming the formation of $Co_2P_2O_7$. The Raman spectrum of the PANI-coated $Co_2P_2O_7$/C is provided in Figure S1, in which the Raman shift at 578 cm^{-1} was allocated to $Co_2P_2O_7$ and the other peaks were attributed to PANI, confirming the successful coating of PANI on $Co_2P_2O_7$. After carbonization, as shown in Figure 2b, there are two distinct Raman peaks: the G-band at 1600 cm^{-1} and the D-band at 1350 cm^{-1},[29] exhibiting the coating of carbon layers. The D-band emerges as a result of the vibration of sp^3 hybridized C and is thus typical of a graphitic plane that is somewhat disordered or flawed. The appearance of the G-band is due to the E2g vibrations of sp^2 hybridized C and hence shows the degree of graphitization.[30,31] The intensity ratio (I_D/I_G) of these two peaks is often used to assess the degree of disorder or defects in graphitic materials.[32] Defects will change the charge distribution of the neighboring carbon, which may be favorable for electrochemical reactions.[33−35] The I_D/I_G of $Co_2P_2O_7$/C @N,P−C at 1.13 is higher than that of the $Co_2P_2O_7$/C catalyst (which is 1.05), suggesting a higher defect degree in $Co_2P_2O_7$/C@N,P−C. As a result, the N-doped carbon coated on $Co_2P_2O_7$/C has a lattice with several defects and disorders.[36]

The surface electronic states and composition of the synthesized catalysts were determined using XPS measurements, and the outcomes are illustrated in Figure 3. The results showed that Co, P, C, and O elements were present in both the $Co_2P_2O_7$/C and $Co_2P_2O_7$/C@N,P−C samples (see Figure 3a). The phosphorization of the phytate derivatives was successful because of the presence of P elements. The PANI resulted in the presence of N in $Co_2P_2O_7$/C@N,P−C. Detailed information on the structure and composition of $Co_2P_2O_7$/C@N,P−C is revealed by the Co 2p, P 2p, N 1s, and C 1s XPS spectra (Figure 3). Co $2p_{3/2}$ and Co $2p_{1/2}$ peaks are situated at 781.3 and 797.4 eV, and 786.1 and 802.7 eV, respectively, in the Co 2p spectra of $Co_2P_2O_7$/C, as depicted in Figure 3b. Compared to the $Co_2P_2O_7$/C NRs, the corresponding peaks of $Co_2P_2O_7$/C@N,P−C in the low-energy direction of Co $2p_{3/2}$ and Co $2p_{1/2}$ are shifted slightly (Figure 2b). This is attributed to the Co electron cloud migration due to the PANI surface-doped nitrogen species' strong electronegativity, which indicates the covalent coupling between $Co_2P_2O_7$/C and the PANI support.[13−15] There is a close association

https://doi.org/10.1021/acsomega.1c05608
ACS Omega 2022, 7, 5751−5763

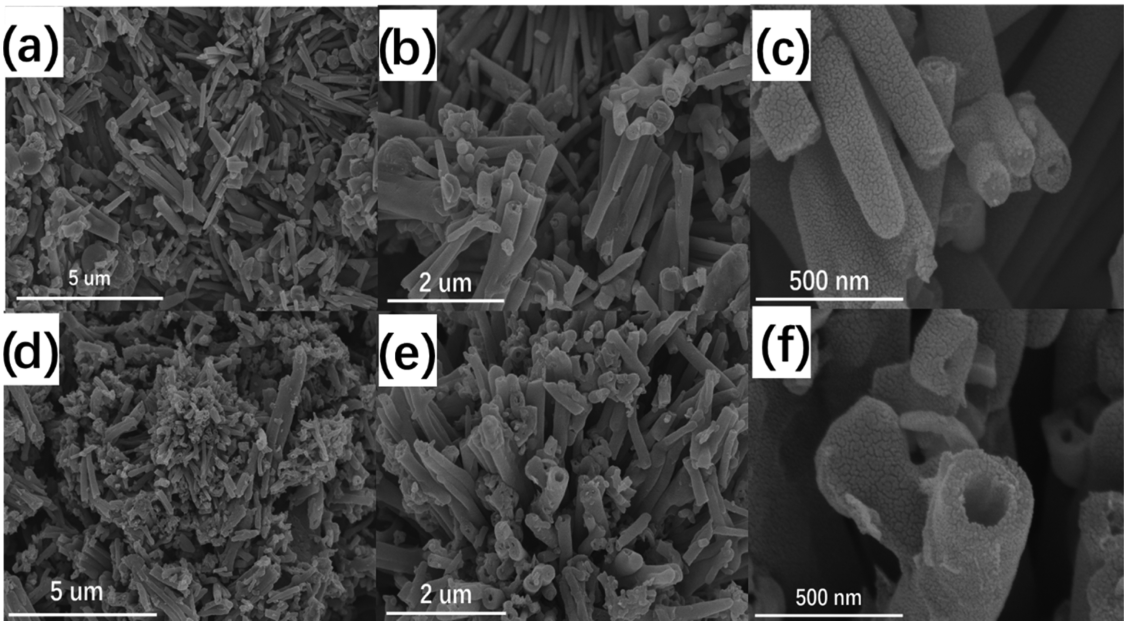

Figure 4. (a–c) Images of SEM for the $Co_2P_2O_7$/C nanorods. (d–f) Images of SEM for the $Co_2P_2O_7$/C@N,P–C nanotubes.

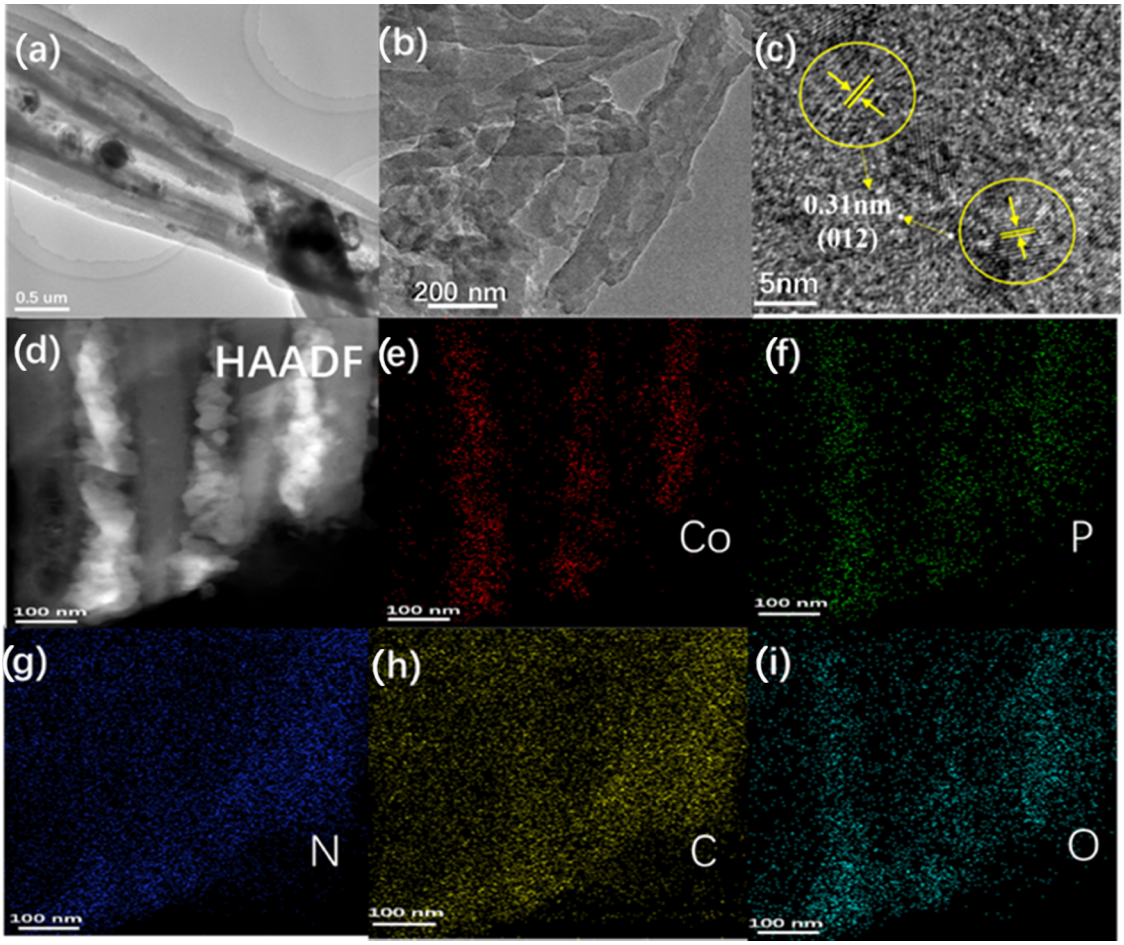

Figure 5. (a, b) Images of TEM for the $Co_2P_2O_7$/C@N,P–C nanocages; (c) image of HRTEM for $Co_2P_2O_7$/C@N,P–C; (d) image of HAADF-STEM as well as (e–i) element-mapping images of a magnified branched region in $Co_2P_2O_7$/C@N,P–C nanotubes.

between these two components, making the catalysts more conductive and electrochemically active, which aims to enhance ORR activity.[37,38] As shown in Figure 3c, the C 1s spectrum of $Co_2P_2O_7$/C@N,P–C contains four distinct peaks, one for aromatic, aliphatic, and graphitic C═C bonds at 284.1 eV, while the peaks at 284.4 and 285.6 eV represent C–C and

https://doi.org/10.1021/acsomega.1c05608
ACS Omega 2022, 7, 5751–5763

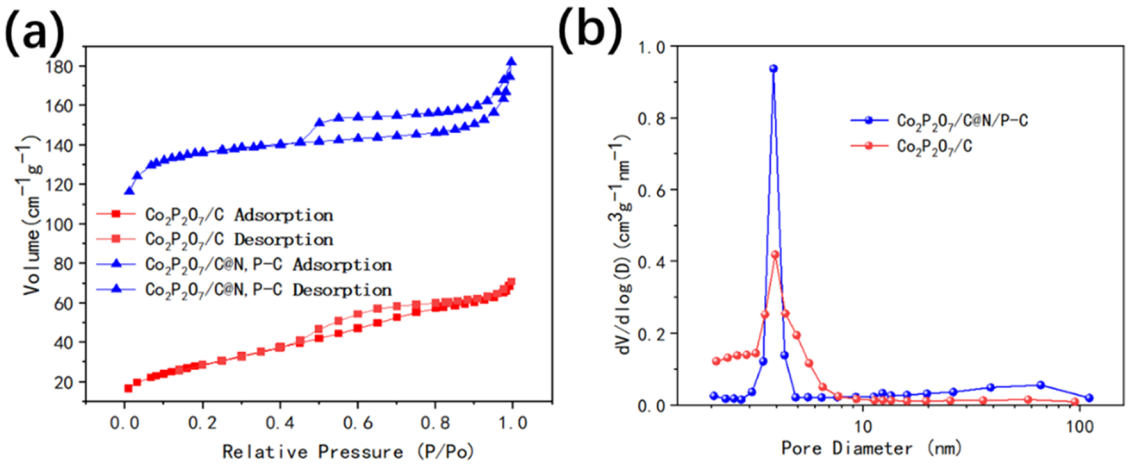

Figure 6. (a)Adsorption−desorption isotherms for N_2 for $Co_2P_2O_7$/C@N,P−C and $Co_2P_2O_7$/C; (b) pore diameter distribution diagram.

C−N bonds, respectively, with one disordered peak at 288.1 eV. During the pyrolysis step, we observed carbon bonds (unsaturated and saturated) in samples, which indicates that PANI graphitization had been successful. In particular, compared to $Co_2P_2O_7$/C, the C−N bond indicates the successful incorporation of N atoms of PANI into the carbon matrix.[39,40] The P 2p peak of $Co_2P_2O_7$/C@N,P−C (Figure 3d) demonstrates three peaks at 133.1, 133.9, and 134.9 eV. The first two peaks correspond to the P $2p_{3/2}$ and P $2p_{1/2}$ phosphate group central phosphorus atom nuclear levels, whereas the latter (134.9 eV) is linked to the phosphorus-like bonding to the carbon lattice structure.[41−44] In the P 2p region of $Co_2P_2O_7$/C, two distinct P species were introduced (Figure 2d). The first (133.5 eV) is because of P atoms chemically bound to O atoms, whereas the second (135.2 eV) is due to P−C coordination. The presence of P−O−P and P−C bonding is in agreement with the FTIR study in Figure S2, in which the vibrations of P−O−P and P−C in the infrared spectrum were attributed to the peaks at 765 and 1076 cm^{-1}, respectively.[28]

The morphology and structure of the synthesized catalysts were then observed with SEM and TEM. The results in Figure 4a−c show that the sample $Co_2P_2O_7$/C is composed of carbon-coated wrapping nanobars ($Co_2P_2O_7$) with a length of over 1 μm and a diameter of approximately 100 nm. However, after the pyrolyzation treatment of the PANI-co-$Co_2P_2O_7$/C precursor, one-dimensional (1D) hollow nanotube catalysts were observed, as shown in Figure 4d,e. Interestingly, the hollow tube structure is more remarkably pronounced with an inner diameter of around 100 nm. This hollowed structure is very beneficial to the penetration of the electrolyte and the transfer of electrons/protons during electrocatalysis. Meanwhile, the rough surface added by the carbon shell provides the potential for efficient mass transport and ion diffusion.

The shape and microstructure of the catalysts, as well as the precursors, were further observed with TEM and high-resolution TEM (HRTEM). The precursor of Co$(CO_3)_{0.5}$(OH)·0.11H_2O nanowires (solid) with a diameter of around 100 nm and different lengths of ~μm can be observed in Figure S3. Then, after the PA was introduced into the solution of Co $(CO_3)_{0.5}$(OH)·0.11H_2O, PA induced decomposition of Co $(CO_3)_{0.5}$(OH)·0.11H_2O, thus resulting in the coordination of Co^{2+} with surface phytate (Co-phytate) with the help of electrostatic attraction. Figure S3c,d shows that an organic layer covered the porous substrates with a thickness of approximately 10 nm, indicating that PA was successfully covered on the surface of Co$(CO_3)_{0.5}$(OH)·0.11H_2O. Figure S4 shows the TEM images of $Co_2P_2O_7$/C, which were obtained by carbonization of the PA-treated Co $(CO_3)_{0.5}$(OH)·0.11H_2O NRs. Interestingly, the rodlike $Co_2P_2O_7$/C with a carbon shell can be seen in Figure S4, and further high-angle annular dark-field scanning transmission electron microscopy (HAADF-STEM) and element-mapping images in Figure S4 verify that the C and P elements are distributed around $Co_2P_2O_7$.

Further, after the carbonization of the PANI-PA-coated $Co_2P_2O_7$/C, as presented in the low-magnification TEM images in Figure 5a, the feature with hollowed nanotube walls was confirmed. The $Co_2P_2O_7$ nanoparticles are wrapped by the hollowed PANI-derived N, P-doped carbon tube. The $Co_2P_2O_7$ nanoparticles are inserted into the carbon skeleton when we magnify the wall (Figure 5b). The lattice fringes show that the 0.31 nm interlayer spacing corresponds to the (012) plane of $Co_2P_2O_7$, which is in agreement with the XRD assessment. The hollow feature is further demonstrated in Figure 5d by the high-angle annular dark-field (HAADF) image and related EDS maps of $Co_2P_2O_7$@N,P−C with uniform distributions of Co, P, and O elements in the inside and N, C elements in the exterior. These findings contribute to the development of a heterogeneous electrocatalyst comprising $Co_2P_2O_7$ nanoparticles embedded in N,P-codoped tubular carbon. According to previous reports on carbon nanostructures wrapping metal or other inorganic nanoparticle hybrids, the introduced carbon layer can not only "armor" the $Co_2P_2O_7$ cores and prevent them from being destroyed during electrochemical cycling but also enhance electron penetration or tunneling and facilitate electrocatalytic application.

N_2 adsorption−desorption tests were employed to assess the specific surface area and porosity of the prepared materials. The BET specific surface area of $Co_2P_2O_7$/C@N,P−C was found to be 459.3 m^2/g, which was greater than that of $Co_2P_2O_7$/C (104.7 m^2/g, Figure 6). The formation of the 1D hollowed tube structure obviously promotes the BET specific surface area. The hierarchical porous structure is noted to have an average pore diameter of 2.63 nm in $Co_2P_2O_7$/C@N,P−C. Meanwhile, the large pore with the diameter close to 80 nm in the pore distribution curve of Figure 6b mainly corresponded to the inner diameter of the formed hollow $Co_2P_2O_7$/C@

https://doi.org/10.1021/acsomega.1c05608
ACS Omega 2022, 7, 5751−5763

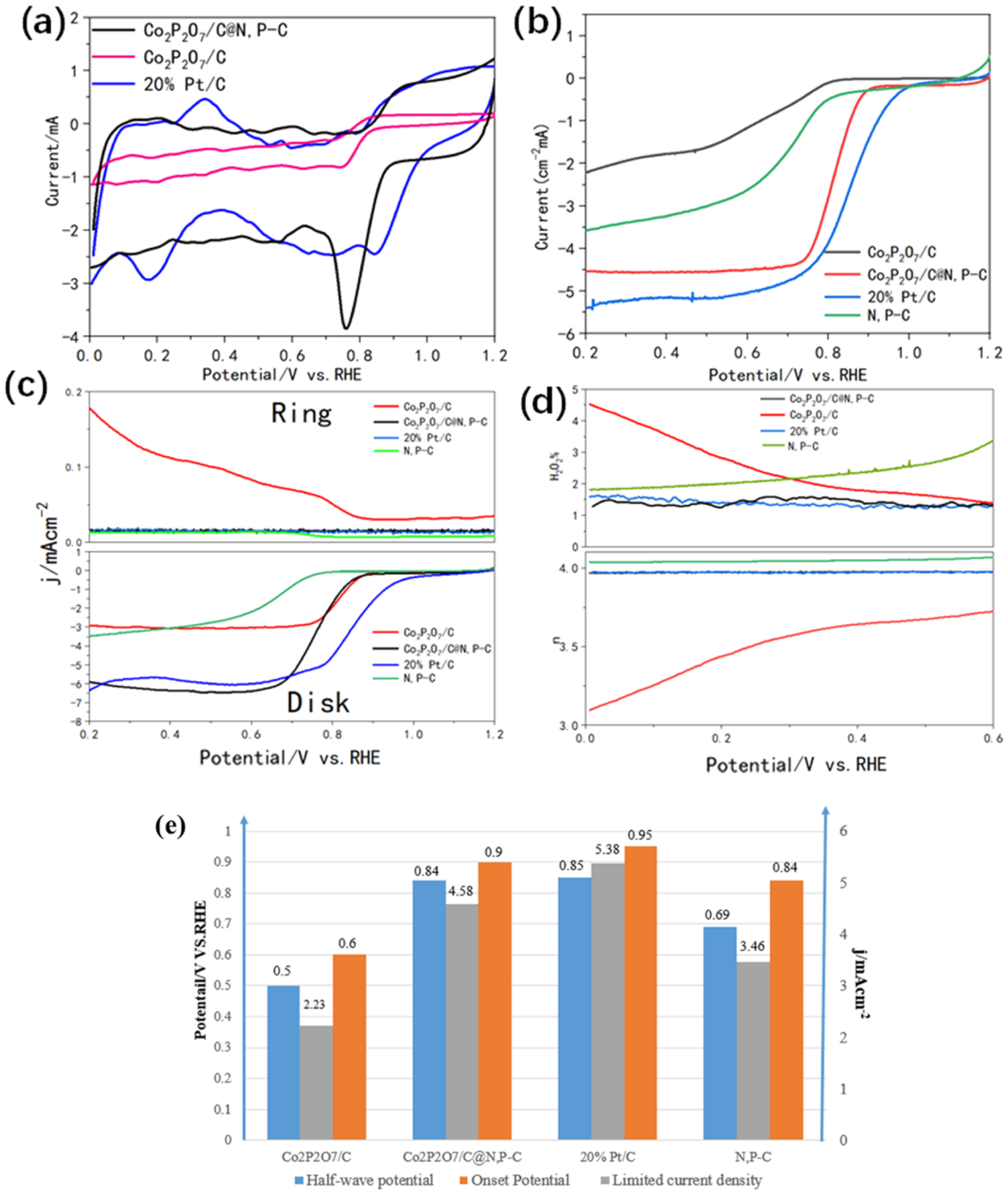

Figure 7. (a) Comparison of the CV of different $Co_2P_2O_7$/C, $Co_2P_2O_7$/C@N,P−C,Co_2P-$Co_2P_2O_7$/C@N,P−C, and 20% Pt/C. (b) LSV curves observed in 0.1 M KOH (O_2-saturated) at 20 and 50 mV/s sweep rates. (c) Curves of RRDE for 20 wt % Pt/C, $Co_2P_2O_7$/C@N, P−C, $Co_2P_2O_7$/C, and PANI-derived N,P−C catalysts. Densities of the ring (upper) and disc (bottom) currents observed at 1600 rpm. (d) Calculated electron transfer numbers *n* for the RRDE data for $Co_2P_2O_7$/C@N,P−C, $Co_2P_2O_7$/C, PANI-derived N,P−C, and 20% Pt/C. (e) Half-wave (blue) and onset (green) potentials together with the restricted current density (gray) values for $Co_2P_2O_7$ /C, $Co_2P_2O_7$/C@N,P−C, Co_2P-$Co_2P_2O_7$/C@ N,P−C, PANI-derived N,P−C, and 20% Pt/C catalysts.

N,P−C tubes. The porous carbon derived from the carbonized PANI matrix as well as the 1D hollowed tube structure was responsible for the increased specific surface area. The hierarchical porous structure develops a specific surface area, which provides numerous energetic spots for the catalytic reaction; meanwhile, porosity facilitates the transfer of reactants, promotes the occurrence of catalytic response, and thus improves the catalytic ability.

3.2. Electrochemical Activity of $Co_2P_2O_7$/C@N,P−C HNTs. To study the electrochemical properties, a three-electrode system was used in an aqueous 0.1 M KOH. The voltage range was 0−0.5 V (relative to RHE). Figure 7a illustrates the curves of CV for $Co_2P_2O_7$/C, $Co_2P_2O_7$/C@ N,P−C, PANI-derived N,P−C, and commercial 20% Pt/C at a scan rate of 50 mV/s. The area around the ring of the CV curve for $Co_2P_2O_7$/C@N,P−C is larger than that of the $Co_2P_2O_7$/C electrode, exhibiting better capacitive performance. LSV tests of $Co_2P_2O_7$/C@N,P−C conducted at 1600 rpm exhibited a diffusion-limited current density of 4.6 mA/cm^2 at 0.2 V (Figure 7c), which is substantially greater than

https://doi.org/10.1021/acsomega.1c05608
ACS Omega 2022, 7, 5751−5763

Table 1. ORR Electrocatalytic Activity Recently Reported for Nonprecious Metal-Based Catalyst Containing Co

	catalyst	electrolyte	onset potential (V)	half-wave potential (V)	limiting current density (mA/cm^2)	refs
1	N−C@CoP	1 M KOH	0.85 V	0.68 V	4.48 mA/cm^2	47
2	CoP/NP-HPC	0.1 M KOH	0.95 V	0.83 V	5.2 mA/cm^2	48
3	NC-CoP	0.1 M KOH	0.82 V	0.69 V	5.2 mA/cm^2	49
4	CoP-DC	0.1 M KOH	N.A.	0.81 V	N.A.	50
5	Co/CoP-HNC	0.1 M KOH	0.93 V	0.83 V	N.A.	51
6	CoP@SNC	1 M KOH	0.87 V	0.79 V	4.8 mA/cm^2	52
7	CoP-PBSCF	0.1 M KOH	N.A.	0.752 V	N.A.	53
8	CoP@PNC-DoS	0.1 M KOH	0.94 V	0.803 V	N.A.	54
9	NPMCNT-300	0.1 M KOH	0.93 V	N.A.	N.A.	55
10	CoP@C	0.1 M KOH	0.91 V	0.87 V	4.2 mA/cm^2	56
11	CoPi/NPGA	0.1 M KOH	0.91 V	0.80	5.1 mA/cm^2	57
12	CoP@PNC-DoS	0.1 M KOH	0.94 V	0.803	N.A.	54
13	$Co_2P_2O_7$/N-rGO-800 (1800 rpm)	0.1 M KOH	0.9 V	0.8	4.7 mA/cm^2	58
14	$Co_2P_2O_7$/C@N,P−C	0.1 M KOH	0.9 V	0.84 V	4.6 mA/cm^2	this work

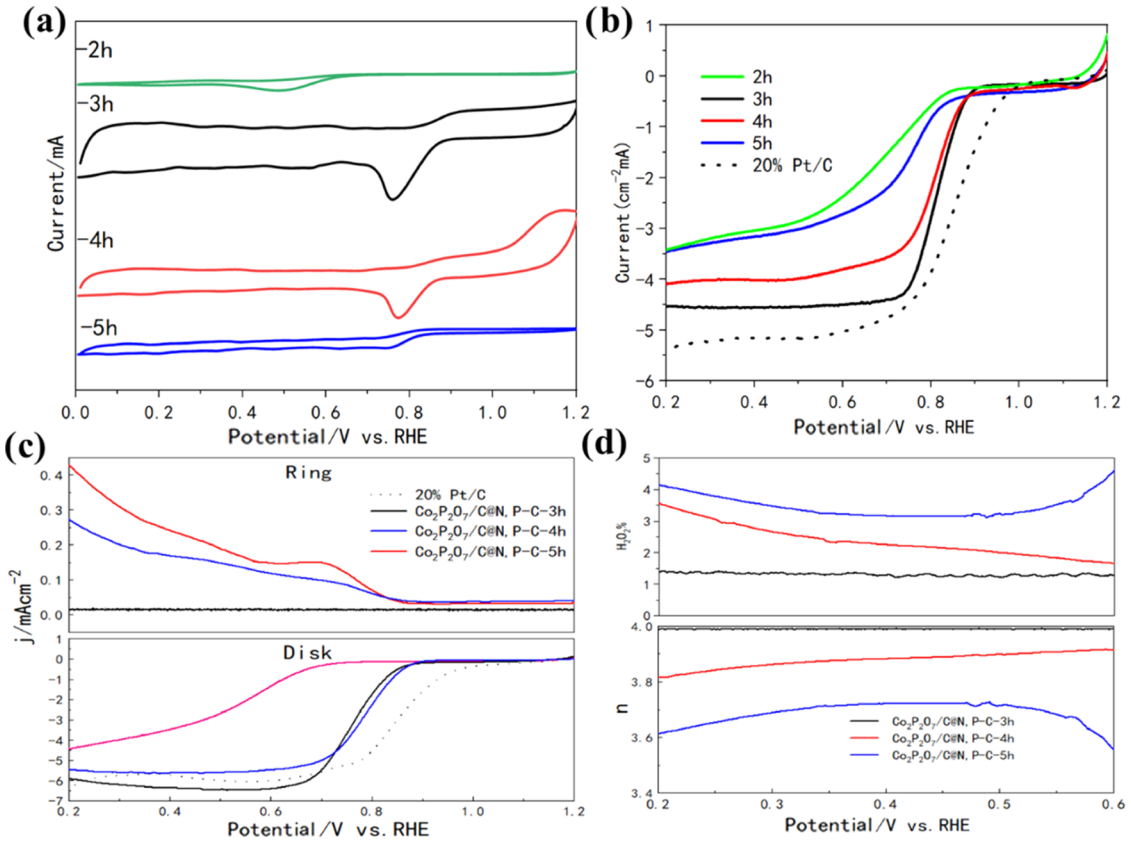

Figure 8. (a) Typical curves of CV for the $Co_2P_2O_7$/C @N,P−C pyrolyzed at different polymerization times in a solution of O_2-saturated 0.1 M KOH with a scan rate of 5 mV/s. (b) LSV recorded in O_2-saturated 0.1 M KOH at 10 and 50 mV/s sweep rates. (c) Curves of RRDE for 20 wt % Pt/C, $Co_2P_2O_7$/C@N,P−C-3h, $Co_2P_2O_7$/C@N,P−C-4h, and $Co_2P_2O_7$/C@N,P−C-5h catalysts. The ring current densities (upper) and disk current densities (bottom) were achieved at 1600 rpm. (d) Evaluated electron transfer numbers *n* for the RRDE data for $Co_2P_2O_7$/C@N,P−C-3h, $Co_2P_2O_7$/C@N,P−C-4h, $Co_2P_2O_7$/C@N,P−C-5h, and 20% Pt/C.

that of $Co_2P_2O_7$/C at 2.23 mA/cm^2 and PANI-derived N,P−C at 3.46 cm^{-2}. A more positive onset potential was observed for $Co_2P_2O_7$/C @N,P−C (equal to 0.91 V) than that of $Co_2P_2O_7$/C at 0.6 V and PANI-derived N,P−C at 0.84 V. The half-wave potential of $Co_2P_2O_7$/C@N,P−C is 0.85 V, and the value is only 50 mV lower than commercial 20 wt % Pt/C catalysts. The ORR pathway was computed, and the OH_2^- ORR yield was screened using RRDE. During ORR with the $Co_2P_2O_7$/C@N,P−C catalyst, the OH_2^- yield was 1.0% (see Figure 7c), and the value of *n* (electron transfer number) was observed in the range of 3.97−3.98, which is quite close to the 20 wt % Pt/C catalyst value. However, the *n* values and OH_2^- yield attained for the $Co_2P_2O_7$/C catalyst-assisted ORR were substantially different from those achieved for the reactions assisted by the 20% Pt/C and $Co_2P_2O_7$/C@N,P−C materials, which demonstrates a four-/two-electron mixed transfer pathway.

In Table 1, we compare the ORR ability of the lately reported $Co_2P_2O_7$-based catalyst with our catalysts. Gratifyingly, the catalyst here reported exhibits a superior perform-

https://doi.org/10.1021/acsomega.1c05608
ACS Omega 2022, 7, 5751−5763

Table 2. Weight Content Prepared at T = 3, 4, and 5 of Pyridinic, Pyrrolic, Oxidized, and Graphitic Nitrogen in the $Co_2P_2O_7$/C@N,P−C-H Catalysts

sample	graphitic-N/N_{total} (%)	pyrrolic-N/N_{total} (%)	pyridinc-N/N_{total} (%)	oxidized-N/N_{total} (%)	graphitic-N + pyridinic-N contents/N_{total} (%)
$Co_2P_2O_7$/C@N,P−C-3h	51.64	21.45	16.51	10.4	68.15
$Co_2P_2O_7$/C@N,P−C-4h	46.88	17.7	5.36	29.06	52.24
$Co_2P_2O_7$/C@N,P−C-5h	21.08	32.22	10.56	20.8	41.88

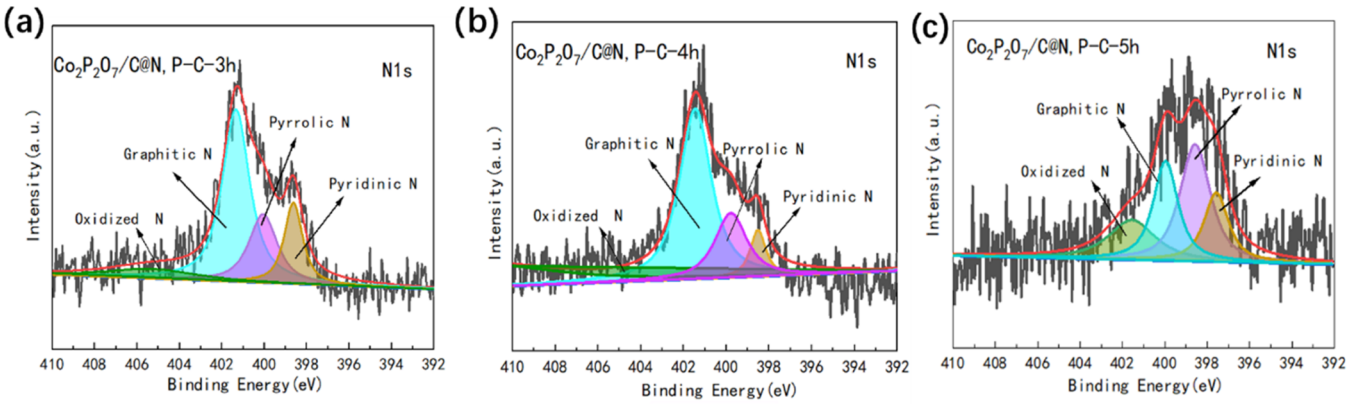

Figure 9. XPS High-resolution N 1s spectra for (a) $Co_2P_2O_7$/C@N,P−C-3h, (b) $Co_2P_2O_7$/C@N,P−C-4h, and (c) $Co_2P_2O_7$/C@N,P−C-5h.

ance no matter the limiting current density and $E_{1/2}$. These findings indicate that the $Co_2P_2O_7$/C@N,P−C materials exhibit an outstanding ORR catalytic activity, which may result from the special hollow tube nanohybrid structure. A synergetic effect of individual components leads to enhancing the ORR movement. In terms of electrocatalytic performance results (Figure 7b), the performance of the composite ternary catalyst is much higher than the performance of PANI-derived N,P-doped C and $Co_2P_2O_7$/C. The $Co_2P_2O_7$ NRs obtained from the $Co(CO_3)_{0.5}(OH)\cdot 0.11H_2O$ precursors are more likely to serve as templates for the fabrication of N,P−C, instead of taking effect in the ORR process. The promising ORR activities of the $Co_2P_2O_7$/C@N,P−C catalysts also highlight the advantages of the exposure of more active sites given by the well-defined 1D hollow nanotube structure and the synergetic interactions between $Co_2P_2O_7$/C and PANI-derived N,P−C in favor of the absorption/desorption of the oxygenated species during the electrocatalytic processes. Moreover, the N,P-doped carbon enhances the specific surface area; thus, the resulting abundant pores and open tunnels permit the facile access of O_2 bubbles and electrolytes toward the active sites to accelerate the ORR process. Further, there also is a considerable electronic coupling effect in the $Co_2P_2O_7$/C and PANI-derived N,P−C components, and electrons can be transferred into the thin C shells from $Co_2P_2O_7$ cores. The conductivity of the catalyst material obtained by four-probe methods was much improved due to the wrapping of PANI-derived N,P−C, with $\sigma_{Co2P2O7/C}$ = 0.468 S/cm up to $\sigma_{Co2P2O7/C@N,P-C}$ = 1.87 S/cm. The thin C shells, in other words, can improve the interfacial electron or electron penetration transfer. Additionally, the pyridinic and graphitic nitrogen atoms with their sp^2 electronic structures are very active ORR sites.[8,45,46] They enhance the material electronic conductivity and increase the catalyst corrosion resistance, which, again, can effectually advance the movement and constancy of the catalysts.

From the above discussion, it is easy to see that the presence of the pyrolytic N,P-doped carbon layer derived from the PANI layer plays an important role in the ORR catalytic performance. A huge improvement of ORR over the original $Co_2P_2O_7$/C was observed. Thus, the effects of polymerized PANI amounts controlled by the polymerization time on the catalyst performance were then investigated.

Figure 8 compares the curves of CV and LSV for $Co_2P_2O_7$/C@N,P-C with different PANI polymerization times during the synthesis process of their carbonized precursors. A distinct cathodic peak can be observed for all of the $Co_2P_2O_7$C@N,P−C samples, which corresponds to the featureless CV curves in O_2-saturated solutions, and the catalytic performance is highly dependent on the quantity of PANI loaded during catalyst preparation. Further, the ORR onset potential of the $Co_2P_2O_7$/C@N,P−C catalyst significantly shifts negatively, and the oxygen reduction current peak dramatically reduced with the increase in polymerization time of PANI. The $Co_2P_2O_7$/C@N,P−C-3h catalyst exhibits the highest overall ORR activity, which is close to that of 20 wt % Pt/C in Figure 8. LSV curves recorded at 1600 rpm show that $Co_2P_2O_7$/C@N,P−C-3h has a higher onset potential (E_{onset}) of 0.90 V vs RHE and a half-wave potential ($E_{1/2}$) of 0.84 V than that of $Co_2P_2O_7$/C@N,P−C-4h and $Co_2P_2O_7$/C@N,P−C 5h, separately (Figure 8b). The polymerization time in the catalyst precursor had a significant influence on the OH_2^- yield and the electron transfer number n attained for the ORR assisted by the $Co_2P_2O_7$/C@N,P−C catalyst. During ORR with the $Co_2P_2O_7$/C@N,P−C-3h catalyst, the OH_2^- yield was 1.0% (see Figure 8c), and the electron transfer number n was in the 3.97−3.98 range, which is extremely similar to the value of the 20 wt % Pt/C catalyst. Moreover, increasing the polymerization duration of PANI in the corresponding precursors resulted in OH_2^- yields and n that were not the same as the ones found in reactions facilitated by 20% Pt/C and $Co_2P_2O_7$C@N,P−C-3h materials, which suggests a two-electron transfer pathway. The weaker presentation of the other catalysts prepared with a longer polymerization time could be explained by the formation of the thicker N-doped

https://doi.org/10.1021/acsomega.1c05608
ACS Omega 2022, 7, 5751−5763

carbon, which is highly confirmed by the following results of XPS and BET measurements.

First, the N1s core-level XPS spectra of the synthesized catalysts were shown in Figure 9, and four types of N bonds were divided. The composed ratio of the different type N was summarized in Table 2. Based on the XPS results, it was noticed that the different N species ratios in the catalysts were strongly influenced by the varied polymerization times of PANI in the catalytic precious that leads to the variety of loaded outside N−C thickness after pyrolysis treatment (see Figure 9 and Table 2). As shown in Table 2, as the polymerization time in the precursor of the $Co_2P_2O_7$/C@N,P-C catalyst enhanced, the total content of graphite N and pyridine N decreased. $Co_2P_2O_7$/C@N,P−C-3h has the greatest total content of graphite N and pyridine N, which is 68.15%. It has been shown that pyridine nitrogen and graphite nitrogen are involved in ORR as active sites, with pyridine nitrogen possessing a pair of lone electrons that can weaken the O−O bond of O_2; thus, it enhanced oxygen adsorption and exhibited better catalytic performance.[8,45,46,59] It can be deduced that the synergistic effects between $Co_2P_2O_7$/C and PANI-derived N,P−C with the active N species (pyridine N, and graphitic N) can effectively reduce the activation barrier of the adsorbed O_2 to promote the capture of the first electron to enhance the cleavage of O−O bonds, thereby improving the ORR activity.[60]

Further, we can see that the specific surface area was also significantly affected through the PANI polarization time. All of the N_2 adsorption−desorption isotherms exhibit the II-type curve in Figure 9, and the BET surface area is compiled in Table 3. The $Co_2P_2O_7$/C@N,P−C-3h catalyst possesses a surface area of 459.30 m^2/g, which is approximately twice that of the $Co_2P_2O_7$/C@N,P−C-4h catalyst, which possesses a surface area of 237.71 m^2/g. The hierarchical porous structure is noticed with an average pore diameter of 4.63 nm in $Co_2P_2O_7$/C@N,P−C. The hierarchical porous structure develops a specific surface area, which provides numerous energetic spots for the catalytic reaction; meanwhile, porosity facilitates the transfer of reactants, promotes the occurrence of catalytic response, and thus improves the catalytic ability (Figures 10 and 11).

Table 3. BET Surface for $Co_2P_2O_7$/C@N,P-C HNTs

	BET surface (m^2/g)	total pore volume (cm^3/g)	average pore diameter (nm)
$Co_2P_2O_7$/C@N,P−C-3h	459.30	0.65	4.63
$Co_2P_2O_7$/C@N,P−C-4h	237.71	0.46	4.52
$Co_2P_2O_7$/C@N,P−C-5h	203.40	0.15	4.58

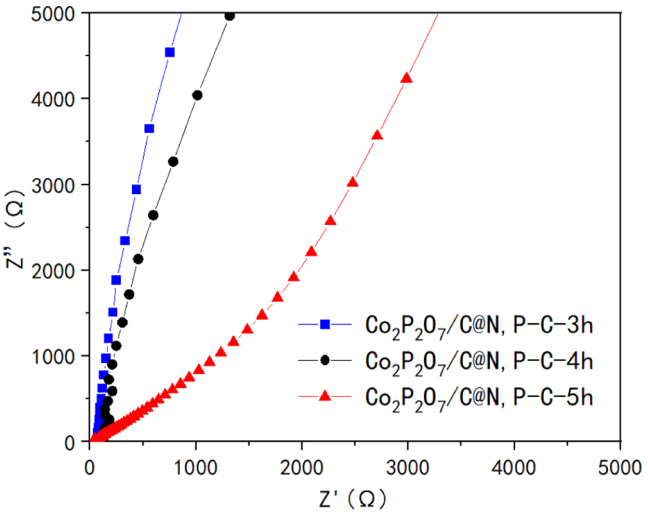

Figure 11. Nyquist plot of $Co_2P_2O_7$/C@N,P−C-3h, $Co_2P_2O_7$/C@N,P−C-4h, and $Co_2P_2O_7$/C@N,P−C-5h catalysts under 0.1 M KOH conditions.

Electrochemical impedance spectroscopy (EIS) measurement Nyquist diagram is one of the effective methods for measuring electrochemically active sites. The Nyquist diagram shows that the slope of the $Co_2P_2O_7$/C@N,P−C-3h catalyst is larger than that of other samples, indicating faster kinetics of charge transfer and an increase in the ion diffusion rate.

We also compared the long-term electrochemical stability of $Co_2P_2O_7$/C@N,P−C and 20% Pt/C catalysts. The *i*−*t*

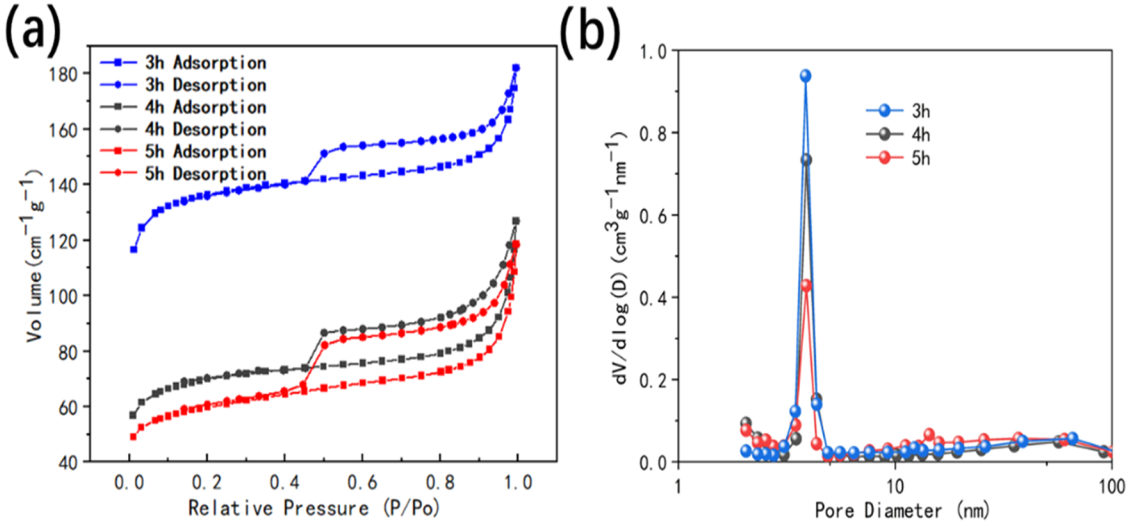

Figure 10. (a) N_2 adsorption−desorption isotherms for $Co_2P_2O_7$/C@N,P−C-3h, $Co_2P_2O_7$/C@N,P−C-4h, and $Co_2P_2O_7$/C@N,P−C-5h and (b) the corresponding pore diameter distribution diagram.

https://doi.org/10.1021/acsomega.1c05608
ACS Omega 2022, 7, 5751−5763

response of $Co_2P_2O_7$/C@N,P−C and Pt/C recorded for 8000 s at 500 rpm is shown in Figure 12. The $Co_2P_2O_7$/C@N,P−C

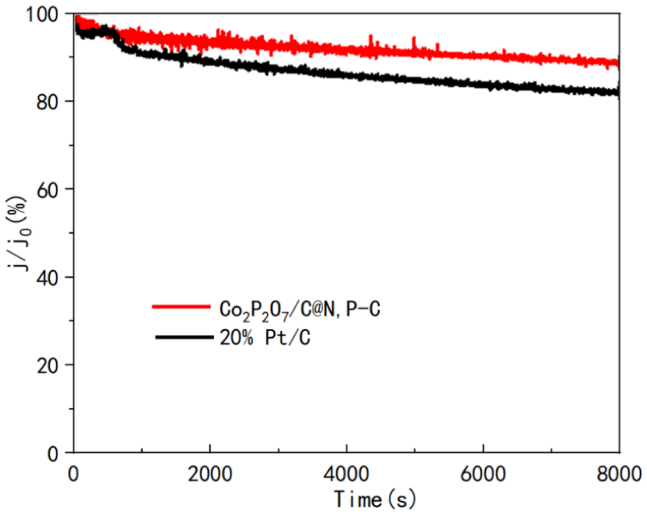

Figure 12. Long-term stability tests performed by the cathodic current−time (i−t) method using $Co_2P_2O_7$/C@N,P−C and 20% Pt/C catalyst performance during ORR.

catalyst exhibited better durability than the commercial Pt/C catalyst: only 9.1% of the activity was lost after 8000 s of a continuous ORR. For comparison, the commercial Pt/C catalyst demonstrated 7.7% lower activity after 8000 s.

5. CONCLUSIONS

To summarize, a simple hydrothermal technique and a subsequent pyrolysis strategy were used to synthesize N,P-rich carbon/carbon $Co_2P_2O_7$ ($Co_2P_2O_7$/C@N,P−C) tubular composite materials. The obtained $Co_2P_2O_7$/C@N,P−C demonstrated a high catalytic activity toward the ORR due to the special hollowed structure and synergistic effect of the $Co_2P_2O_7$ and PANI-derived N,P-doped C. The onset and positive half-wave potentials were recorded at 0.90 and 0.84 V, respectively, while the diffusion-limited current density was 4.6 mA/cm^2, values that were similar to those of commercial 20% Pt/C. The $Co_2P_2O_7$/C@N,P−C catalyst also has excellent stability compared to 20% Pt/C. It was demonstrated that the specific surface area, as well as the content of graphitic N, changed with the time of PANI polymerization, resulting in a significantly different catalytic performance, and an optimal value was achieved with 3 h of PANI polymerization in its precursor. This investigation of hollow tube metal phosphate-based materials reveals significant potential for energy storage regeneration and conversion technologies.

■ ASSOCIATED CONTENT

Supporting Information

The Supporting Information is available free of charge at https://pubs.acs.org/doi/10.1021/acsomega.1c05608.

Raman data of Co $(CO_3)_{0.5}(OH)\cdot 0.11H_2O$, Co $(CO_3)_{0.5}(OH)\cdot 0.11H_2O$ @PA, and $Co_2P_2O_7$/C@PANI; FTIR data of $Co_2P_2O_7$/C and $Co_2P_2O_7$/C@N,P−C; TEM information of $Co(CO_3)_{0.5}(OH)\cdot 0.11H_2O$ and $Co(CO_3)_{0.5}(OH)\cdot 0.11H_2O$@PA; and TEM and STEM-EDS mapping results of $Co_2P_2O_7$/C (PDF)

■ AUTHOR INFORMATION

Corresponding Authors

Yanhua Lei − *Institute of Marine Materials Science and Engineering, Shanghai Maritime University, Shanghai 201306, China;* orcid.org/0000-0001-8850-3531; Email: yhlei@shmtu.edu.cn

Hailiang Du − *College of Mechanical and Electronic Engineering, Shanghai Jian Qiao University, Shanghai 201315, China*; Email: hailiang_du@hotmail.com

Authors

Da Huo − *Institute of Marine Materials Science and Engineering, Shanghai Maritime University, Shanghai 201306, China*

Mengchao Ding − *Institute of Marine Materials Science and Engineering, Shanghai Maritime University, Shanghai 201306, China*

Fei Zhang − *Institute of Marine Materials Science and Engineering, Shanghai Maritime University, Shanghai 201306, China*

Ruixuan Yu − *National Laboratory of Solid State Microstructures, College of Engineering and Applied Sciences, Nanjing University, Nanjing 210023, China*

Yuliang Zhang − *Institute of Marine Materials Science and Engineering, Shanghai Maritime University, Shanghai 201306, China;* orcid.org/0000-0001-7205-7768

Complete contact information is available at: https://pubs.acs.org/10.1021/acsomega.1c05608

Notes

The authors declare no competing financial interest.

■ ACKNOWLEDGMENTS

This work was supported by the National Natural Science Foundation of China (NSFC Grant Nos. 51602195 and 11804152), the Natural Science Foundation of Shanghai (Grant No. 19ZR1422200), and the Foundation of Shanghai Engineering Technology Research Centre of Deep Offshore Material (19DZ2253100).

■ REFERENCES

(1) Gewirth, A. A.; Thorum, M. S.; Matthew, S. Electroreduction of Dioxygen for Fuel-Cell Applications: Materials and Challenges. *Inorg. Chem.* **2010**, *49*, 3557−3566.

(2) Miotti, M.; Hofer, J.; Bauer, C. Integrated environmental and economic assessment of current and future fuel cell vehicles. *Int. J. Life Cycle Assess* **2017**, *22*, 94−110.

(3) Li, Y.; Gong, M.; Liang, Y.; Feng, J.; Dai, H.; et al. Advanced zinc-air batteries based on high-performance hybrid electrocatalysts. *Nat. Commun.* **2013**, *4*, No. 1805.

(4) Zhang, J.; Sasaki, K.; Sutter, E.; Adzic, R. R. Stabilization of Platinum Oxygen-Reduction Electrocatalysts Using Gold Clusters. *Science* **2007**, *5809*, 220−222.

(5) Yu, X.; Ye, S. Recent advances in activity and durability enhancement of Pt/C catalytic cathode in PEMFC: Part II: Degradation mechanism and durability enhancement of carbon supported platinum catalyst. *J. Power Sources* **2007**, *172*, 133−144.

(6) Shao, Y.; Yin, G.; Gao, Y. Understanding and approaches for the durability issues of Pt-based catalysts for PEM fuel cell. *J. Power Sources* **2007**, *171*, 558−566.

(7) Gong, K.; Du, F.; Xia, Z.; Durstock, M.; Dai, L. Nitrogen-doped carbon nanotube arrays with high electrocatalytic activity for oxygen reduction. *Science* **2009**, *323*, 760−764.

https://doi.org/10.1021/acsomega.1c05608
ACS Omega 2022, 7, 5751−5763

(8) Guo, D.; Shibuya, R.; Akiba, C.; Saji, S.; Kondo, T.; Nakamura, J. Active sites of nitrogen-doped carbon materials for oxygen reduction reaction clarified using model catalysts. *Science* **2016**, *351*, 361−365.
(9) Yang, F.; Zhao, P.; Hua, X.; Luo, W.; Cheng, G.; Xing, W.; Chen, S. A cobalt-based hybrid electrocatalyst derived from a carbon nanotube inserted metal−organic framework for efficient water-splitting. *J. Mater. Chem. A* **2016**, *4*, 16057−16063.
(10) Zhang, R.; He, S.; Lu, Y.; Chen, W. Fe, Co, N-functionalized carbon nanotubes in situ grown on 3D porous N-doped carbon foams as a noble metal-free catalyst for oxygen reduction. *J. Mater. Chem. A* **2015**, *3*, 3559−3567.
(11) Chung, H. T.; Cullen, D. A.; Higgins, D.; Sneed, B. T.; Holby, E. F.; More, K. L.; Zelenay, P. Direct atomic-level insight into the active sites of a high-performance PGM-free ORR catalyst. *Science* **2017**, *357*, 479.
(12) Liu, T.; Zhao, P.; Hua, X.; Luo, W.; Chen, S.; Cheng, G. An Fe−N−C hybrid electrocatalyst derived from a bimetal−organic framework for efficient oxygen reduction. *J. Mater. Chem. A* **2016**, *4*, 11357−11364.
(13) Bu, L.; Zhang, N.; Guo, S.; Zhang, X.; Li, J.; Yao, J.; Wu, T.; Lu, G.; Ma, J.-Y.; Su, D.; Huang, X. Biaxially strained PtPb/Pt core/shell nanoplate boosts oxygen reduction catalysis. *Science* **2016**, *354*, 1410−1414.
(14) Pour-Ali, S.; Dehghanian, C.; Kosari, A. In situ synthesis of polyaniline−camphorsulfonate particles in an epoxy matrix for corrosion protection of mild steel in NaCl solution. *Corros. Sci.* **2014**, *85*, 204−214.
(15) Wang, X.; Zhuang, L.; He, T.; Jia, Y.; Zhang, L.; Yan, X.; Gao, M.; Du, A.; Zhu, Z.; Yao, X.; Yu, S.-H. Grafting Cobalt Diselenide on Defective Graphene for Enhanced Oxygen Evolution Reaction. *iScience* **2018**, *7*, 145−153.
(16) Zhang, J.; Qu, L.; Shi, G.; Liu, J.; Chen, J.; Dai, L. N, P-Codoped Carbon Networks as Efficient Metal-free Bifunctional Catalysts for Oxygen Reduction and Hydrogen Evolution Reactions. *Angew. Chem., Int. Ed.* **2016**, *55*, 2230−2234.
(17) Gao, K.; Wang, B.; Tao, L.; Cunning, B. V.; Zhang, Z.; Wang, S.; Ruoff, R. S.; Qu, L. Efficient Metal-Free Electrocatalysts from N-Doped Carbon Nanomaterials: Mono-Doping and Co-Doping. *Adv. Mater.* **2018**, *31*, No. 1805121.
(18) Zhu, Y. P.; Jing, Y.; Vasileff, A.; Heine, T.; Qiao, S. Z. 3D Synergistically Active Carbon Nanofibers for Improved Oxygen Evolution. *Adv. Energy Mater.* **2017**, *7*, No. 1602928.
(19) Jiang, W.-J.; Gu, L.; Li, L.; Zhang, Y.; Zhang, X.; Zhang, L.-J.; Wang, J.-Q.; Hu, J.-S.; Wei, Z.; Wan, L.-J. Understanding the High Activity of Fe-N-C Electrocatalysts in Oxygen Reduction: Fe/Fe3C Nanoparticles Boost the Activity of Fe-N(x). *J. Am. Chem. Soc.* **2016**, *138*, 3570−3578.
(20) Hou, L. R.; Lian, L.; Li, D. K.; Lin, J. D.; Pan, G.; Zhang, L. H.; Zhang, X. G.; Zhang, Q. G.; Yuan, C. Z. Facile synthesis of Co2P2O7 nanorods as a promising pseudocapacitive material towards high-performance electrochemical capacitors. *RSC Adv.* **2013**, *3*, 21558−21562.
(21) Wang, F. M.; Zhao, H. M.; Ma, Y. R.; Yang, Y.; Li, B.; Cui, Y. Y.; Guo, Z. Y.; Wang, L. Core-shell-structured Co@Co4N nanoparticles encapsulated into MnO-modified porous N-doping carbon nanocubes as bifunctional catalysts for rechargeable Zn-air batteries. *J. Energy Chem.* **2020**, *50*, 52−62.
(22) Wang, Y. Z.; Wang, B.; Yuan, H. T.; Liang, Z. Z.; Huang, Z. H.; Zhou, Y. Y.; Zhang, W.; Zheng, H. Q.; Cao, R. Inherent mass transfer engineering of a Co, N co-doped carbon material towards oxygen reduction reaction. *J. Energy Chem.* **2021**, *58*, 391−396.
(23) Tong, X.; Chen, S.; Guo, C.; Xia, X.; Guo, X. Y. Mesoporous NiCo2O4 Nanoplates on Three-Dimensional Graphene Foam as an Efficient Electrocatalyst for the Oxygen Reduction Reaction. *ACS Appl. Mater. Interfaces* **2016**, *8*, 28274.
(24) Yang, J.; Sun, H.; Liang, H.; Ji, H.; Song, L. A Highly Efficient Metal-Free Oxygen Reduction Electrocatalyst Assembled from Carbon Nanotubes and Graphene. *Adv. Mater.* **2016**, *28*, 4606.
(25) Hu, J.; Gan, M.; Ma, L.; Li, Z.; Yan, J.; Zhang, J. Synthesis and anticorrosive properties of polymer−clay nanocomposites via chemical grafting of polyaniline onto Zn-Al layered double hydroxides. *Surf. Coat. Technol.* **2014**, *240*, 55−62.
(26) Yang, Z. K.; Lin, L.; Liu, Y.-N.; Zhou, X.; Yuan, C.-Z.; Xu, A.-W. Supramolecular polymers-derived nonmetal N, S-codoped carbon nanosheets for efficient oxygen reduction reaction. *RSC Adv.* **2016**, *6*, 52937−52944.
(27) Lei, Y.; Tan, N.; Zhu, Y.; Huo, D.; Gao, G.; et al. Synthesis of Porous N-Rich Carbon/MXene from MXene@Polypyrrole Hybrid Nanosheets as Oxygen Reduction Reaction Electrocatalysts. *J. Electrochem. Soc.* **2020**, *167*, No. 116503.
(28) Harcharras, M.; Ennaciri, A.; Capitelli, F.; Mattei, G. Vibrational spectra and thermal dehydration of $Co_2P_2O_7 \cdot 6H_2O$ diphosphate. *Vib. Spectrosc.* **2003**, *33*, 189−196.
(29) Ren, L. L.; Wang, Y. M.; Wu, Z. Q.; Xiang, Z. C.; Guo, L.; et al. Identification of a novel coronavirus causing severe pneumonia in human: a descriptive study. *Chin. Med. J.* **2020**, *133*, 1015−1024.
(30) An, H.; Zhang, R.; Li, Z.; Zhou, L.; Shao, M.; Wei, M. Highly efficient metal-free electrocatalysts toward oxygen reduction derived from carbon nanotubes@polypyrrole core−shell hybrids. *J. Mater. Chem. A* **2016**, *4*, 18008−18014.
(31) Ye, B.; Cheng, K.; Li, W.; Liu, J.; Zhang, J.; Mu, S. Polyaniline and Perfluorosulfonic Acid Co-Stabilized Metal Catalysts for Oxygen Reduction Reaction. *Langmuir* **2017**, *33*, 5353−5361.
(32) Qiao, Y.; Li, C. M. Nanostructured catalysts in fuel cells. *J. Mater. Chem.* **2011**, *21*, 4027−4036.
(33) Yan, D.; Li, Y.; Huo, J.; Chen, R.; Dai, L.; Wang, S. Defect Chemistry of Nonprecious-Metal Electrocatalysts for Oxygen Reactions. *Adv. Mater.* **2017**, *29*, No. 1606459.
(34) Lin, Y.; Yang, L.; Zhang, Y.; Jiang, H.; Xiao, Z.; Wu, C.; Zhang, G.; Jiang, J.; Song, L. Defective Carbon−CoP Nanoparticles Hybrids with Interfacial Charges Polarization for Efficient Bifunctional Oxygen Electrocatalysis. *Adv. Energy Mater.* **2018**, *8*, No. 1703623.
(35) Yan, X.; Jia, Y.; Yao, X. Defects on carbons for electrocatalytic oxygen reduction. *Chem. Soc. Rev.* **2018**, *47*, 7628−7658.
(36) Shi, Q.; Ma, Y.; Qin, L.; Tang, B.; Yang, W. Y.; Liu, Q. Metal-Free Hybrid of Nitrogen-Doped Nanocarbon@Carbon Networks for Highly Efficient Oxygen Reduction Electrocatalyst. *ChemElectroChem* **2019**, *6*, 2924−2930.
(37) Xu, H.; Wang, A.-L.; Tong, Y.-X.; Li, G.-R. Enhanced Catalytic Activity and Stability of Pt/CeO2/PANI Hybrid Hollow Nanorod Arrays for Methanol Electro-oxidation. *ACS Catal.* **2016**, *6*, 5198−5206.
(38) Kakinuma, K.; Chino, Y.; Senoo, Y.; Uchida, M.; Kamino, T.; Uchida, H.; Deki, S.; Watanabe, M. Characterization of Pt catalysts on Nb-doped and Sb-doped SnO2−δ support materials with aggregated structure by rotating disk electrode and fuel cell measurements. *Electrochim. Acta* **2013**, *110*, 316−324.
(39) Zhang, S.; Chen, S. Enhanced-electrocatalytic activity of Pt nanoparticles supported on nitrogen-doped carbon for the oxygen reduction reaction. *J. Power Sources* **2013**, *240*, 60−65.
(40) Liu, L.; Zeng, G.; Chen, J.; Bi, L.; Dai, L.; Wen, Z. N-doped porous carbon nanosheets as pH-universal ORR electrocatalyst in various fuel cell devices. *Nano Energy* **2018**, *49*, 393−402.
(41) Li, Y.; Gong, M.; Liang, Y.; Feng, J.; Kim, J.-E.; Wang, H.; Hong, G.; Zhang, B.; Dai, H. Advanced zinc-air batteries based on high-performance hybrid electrocatalysts. *Nat. Commun.* **2013**, *4*, No. 1805.
(42) Zhu, Y.-P.; Xu, X.; Su, H.; Liu, Y.-P.; Chen, T.; Yuan, Z.-Y. Ultrafine Metal Phosphide Nanocrystals in Situ Decorated on Highly Porous Heteroatom-Doped Carbons for Active Electrocatalytic Hydrogen Evolution. *ACS Appl. Mater. Interfaces* **2015**, *7*, 28369−28376.
(43) Cao, S. B.; Qu, T.; Zhang, A.; Zhao, Y. B.; Chen, A. H. N-Doped Hierarchical Porous Carbon with Open-Ended Structure for High-Performance Supercapacitors. *ChemElectroChem* **2019**, *6*, 1696−1703.

https://doi.org/10.1021/acsomega.1c05608
ACS Omega 2022, 7, 5751−5763

(44) Zhu, Y. P.; Liu, Y. L.; Liu, Y. P.; Ren, T. Z.; Chen, T. H.; Yuan, Z. Y. Direct Synthesis of Phosphorus-Doped Mesoporous Carbon Materials for Efficient Electrocatalytic Oxygen Reduction. *ChemCatChem* **2015**, *7*, 2903−2909.
(45) Wütscher, A.; Eckhard, T.; Hiltrop, D.; Lotz, K.; Schuhmann, W.; Andronescu, C.; Muhler, M. Nitrogen-Doped Metal-Free Carbon Materials Derived from Cellulose as Electrocatalysts for the Oxygen Reduction Reaction. *ChemElectroChem* **2019**, *6*, 514−521.
(46) Deng, H.; Li, Q.; Liu, J.; Wang, F. Active sites for oxygen reduction reaction on nitrogen-doped carbon nanotubes derived from polyaniline. *Carbon* **2017**, *112*, 219−229.
(47) Khalafallah, D.; Othman, Y.; Fouad, H.; Khalil, A. K. Nitrogen and carbon functionalized cobalt phosphide as efficient non-precious electrocatalysts for oxygen reduction reaction electrocatalysis in alkaline environment. *J. Electroanal. Chem.* **2018**, *809*, 96−104.
(48) Wang, Y.; Wu, M.; Li, J.; Huang, H.; Qiao, J. In situ growth of CoP nanoparticles anchored on (N,P) co-doped porous carbon engineered by MOFs as advanced bifunctional oxygen catalyst for rechargeable Zn−air battery. *J. Mater. Chem. A* **2020**, *8*, 19043−19049.
(49) Kumar, M. M.; Raj, C. R. Carbothermal-Reduction-Assisted Phosphidation of Cobalt Affords Mesoporous Nitrogen-Doped Carbon-Embedded CoP Nano electrocatalysts for the Oxygen Reduction Reaction. *ACS Appl. Nano Mater.* **2019**, *2*, 643−648.
(50) Lin, Y.; Yang, L.; Zhang, Y.; Jiang, H.; Xiao, Z. Defective Carbon-CoP Nanoparticles Hybrids with Interfacial Charges Polarization for Efficient Bifunctional Oxygen Electrocatalysis. *Adv. Energy Mater.* **2018**, *8*, No. 1703623.
(51) Hao, Y. C.; Xu, Y. Q.; Liu, W.; Sun, X. M. Co/CoP embedded in a hairy nitrogen-doped carbon polyhedron as an advanced trifunctional electrocatalyst. *Mater. Horiz.* **2018**, *5*, 108−115.
(52) Meng, T.; Hao, Y. N.; Zheng, L. R.; Cao, M. H. Organophosphoric acid-derived CoP quantum dots@S,N-codoped graphite carbon as a trifunctional electrocatalyst for overall water splitting and Zn-air batteries. *Nanoscale* **2018**, *10*, 14613−14626.
(53) Zhang, Y. Q.; Tao, H. B.; Chen, Z.; Li, M.; Luo, J. L.; et al. In situ grown cobalt phosphide (CoP) on perovskite nanofibers as an optimized trifunctional electrocatalyst for Zn−air batteries and overall water splitting. *J. Mater. Chem. A* **2019**, *7*, 26607−26617.
(54) Li, Y.; Liu, Y.; Qian, Q.; Wang, G.; Zhang, G. Supramolecular assisted one-pot synthesis of donut-shaped CoP@PNC hybrid nanostructures as multifunctional electrocatalysts for rechargeable Zn-air batteries and self-powered hydrogen production - ScienceDirect. *Energy Storage Mater.* **2020**, *28*, 27−36.
(55) Yang, X.; Mi, H.; Ren, X.; Zhang, P.; Li, Y. Co/CoP Nanoparticles Encapsulated Within N, P-Doped Carbon Nanotubes on Nanoporous Metal-Organic Framework Nanosheets for Oxygen Reduction and Oxygen Evolution Reactions. *Nanoscale Res. Lett.* **2020**, *15*, No. 82.
(56) Ingavale, S.; Patil, I.; Prabakaran, K.; Swami, A. Microwave-assisted synthesis of cobalt-polyoxometalate@carbon black nanocomposites and their electrocatalytic ability toward oxygen reduction reaction. *Int. J. Energy Res.* **2021**, *45*, 7366−7379.
(57) Ren, J. T.; Yuan, G. G.; Chen, L.; Weng, C. C.; Yuan, Z. Y. Rational Dispersion of Co2P2O7 Fine Particles on N,P-Codoped Reduced Graphene Oxide Aerogels Leading to Enhanced Reversible Oxygen Reduction Ability for Zn-Air Batteries. *ACS Sustainable Chem. Eng.* **2018**, *6*, 9793−9803.
(58) Li, K.; Guo, M.; Yan, Y.; Zhan, K.; Yang, J.; Zhao, B.; Li, J. Ultrasmall Co2P2O7 nanocrystals anchored on nitrogen-doped graphene as efficient electrocatalysts for the oxygen reduction reaction. *New J. Chem.* **2019**, *43*, 6492−6499.
(59) Lei, Y. H.; Ning, T.; Da, H.; Ding, M. C.; Zhang, Y. L.; Tong, L.; Yu, R. X.; Sha, C.; Fan, R. H. Fabrication of Porous N-rich Carbon Electrocatalysts from Pyrolysis of PANI-Encapsulated CeO_2 for Enhanced Oxygen Reduction Reaction. *J. Electrochem. Soc.* **2021**, *168*, No. 044516.
(60) Liu, B.; Wang, R.; Yao, Y.; Ma, J.; Sun, Y.; Wan, J.; Zhang, Y.; Wang, S.; Zou, J. Hollow-structured CoP nanotubes wrapped by N-doped carbon layer with interfacial charges polarization for efficiently boosting oxygen reduction/evolution reactions. *Chem. Eng. J.* **2021**, *431*, No. 133238.

https://doi.org/10.1021/acsomega.1c05608
ACS Omega 2022, 7, 5751−5763